Research Article | Vol. 12, No. 9 / 1 Sep 2021 / Biomedical Optics Express 5704
Biomedical Optics EXPRESS

All-fiber few-mode optical coherence tomography using a modally-specific photonic lantern

MARTIN POINSINET DE SIVRY-HOULE,[1] SIMON BOLDUC BEAUDOIN,[2] SIMON BRAIS-BRUNET,[3] MATHIEU DEHAES,[3,4,5] NICOLAS GODBOUT,[1] AND CAROLINE BOUDOUX[1,5,*]

[1] *Polytechnique Montréal, Engineering Physics Department, Montréal (QC), Canada*
[2] *Université de Sherbrooke, Physics Department, Sherbrooke (QC), Canada*
[3] *Université de Montréal, Institute of Biomedical Engineering, Montréal (QC), Canada*
[4] *Université de Montréal, Department of Radiology, Radio-oncology and Nuclear Medicine, Montréal (QC), Canada*
[5] *Research Centre, CHU Ste-Justine, Montréal (QC), Canada*
[*] *caroline.boudoux@polymtl.ca*

Abstract: Optical coherence tomography (OCT) was recently performed using a few-mode (FM) fiber to increase contrast or improve resolution using a sequential time-domain demultiplexing scheme isolating the different interferometric signals of the mode-coupled backscattered light. Here, we present an all-fiber FM-OCT system based on a parallel modal demultiplexing scheme exploiting a novel modally-specific photonic lantern (MSPL). The MSPL allows for maximal fringe visibility for each fiber propagation mode in an all-fiber assembly which provides the robustness required for clinical applications. The custom-built MSPL was designed for OCT at 930 nm and is wavelength-independent over the broad OCT spectrum. We further present a comprehensive coupling model for the interpretation of FM-OCT images using the first two propagation modes of a few-mode fiber, validate its predictions, and demonstrate the technique using *in vitro* microbead phantoms and *ex vivo* biological samples.

1. Introduction

Optical coherence tomography (OCT) is an imaging technique that relies on low-coherence interferometry to measure depth-resolved reflectance profiles of tissues [1]. By illuminating a sample with a low-coherence light source, OCT systems measure the cross-correlation signal with a reference arm to discriminate backscattering light originating from different tissue depths. This discrimination, which is called coherence gating, allows obtaining a three-dimensional reconstruction of the sample. Similar to most microscopy techniques, OCT comprises an illumination and a collection scheme. Typically, OCT systems use a unique single-mode fiber (SMF) for both illumination and collection, thereby rejecting most backscattered light along with information it carries. Several optical techniques — including elastic light scattering spectroscopy [2] and hybrid confocal imaging [3] — exploit this wealth of information as a contrast mechanism. However, these techniques are constrained to probing thin samples to ensure a single-scattering regime, as multiple-scattering would randomize the phase function. By comparison, the intrinsic coherence gating of OCT can be used to assess scattering in a thin, virtual layer located within a macroscopic sample. Therefore, combining OCT imaging with a contrast mechanism based on the scattering phase function (SPF) would allow exploiting valuable information including in-depth intrinsic properties of the biological tissue.

Previous studies have shown that this strategy could be achieved using the first few propagation modes of a few-mode fiber (FMF) provided they can be efficiently isolated and independently

#428101 https://doi.org/10.1364/BOE.428101
Journal © 2021 Received 26 Apr 2021; revised 29 Jun 2021; accepted 21 Jul 2021; published 19 Aug 2021

Biomedical Optics EXPRESS

measured [4,5]. In particular, these studies suggest that contrast channels based on scattering directionality can be obtained using higher-order propagation modes. Amongst other things, they demonstrated the use of higher-order modes to highlight neuritic plaques associated with Alzheimer's disease in *ex vivo* brain samples. The optical system previously described [4] exploits modal dispersion of an FMF [6] to achieve time-windowing demultiplexing of the interferometric channels. However, the complex scheme proposed by the authors presents technical limitations on maximal fringe visibility. In particular, as the scheme requires free-space misalignment of the optical beam to allow for interference between orthogonal modes, the acquisition of additional modes requires increasing the offset at the expense of the signal-to-noise ratio. To simplify the imaging system and overcome these limitations, we present an all-fiber approach based on a custom-made MSPL. Photonic lanterns are N-by-one fiber optic components mapping the propagation modes of a bundle of N SMFs to the modes of a multimode structure [7]. MSPLs are a sub-category of photonic lanterns that feature a one-to-one mapping between individual SMFs and linearly polarized (LP) modes of a multimode fiber. Reciprocally, MSPLs allow demultiplexing the modal content of light propagating in a multimode fiber. MSPLs are intrinsically wavelength independent. This signifies that the modal mapping does not depend on the excitation wavelength, a trait that makes them particularly interesting for broadband imaging techniques such as OCT. Figure 1 presents a schematic describing the principle of a MSPL. In particular, Fig. 1(a) shows the excitation in the upper SMF mapping to the fundamental mode of an FMF, while in Fig. 1(b), the lower SMF maps to a higher order mode of the FMF. In this paper, we present a few-mode OCT imaging system based on a custom-designed MSPL, provide a comprehensive model for the mode-dependent coupling mechanism of the backscattered light onto the FMF, and experimentally validate numerical predictions through responses from optical phantoms and *ex vivo* biological samples.

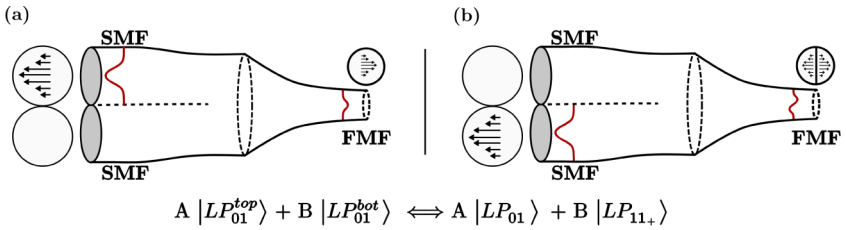

Fig. 1. Schematic of a modally-specific photonic lantern. (a) The top SMF linearly-polarized (LP) mode, $|LP_{01}^{top}\rangle$, maps the LP_{01} mode of an FMF. (b) The bottom SMF mode, $|LP_{01}^{bot}\rangle$, maps the LP_{11+} mode of the FMF. Mapping from the FMF to the SMF is reciprocal. The equation shows the mapping relation with A and B being amplitude coefficients, and the + sign (as opposed to $\times$) represents one of the two orthogonal LP_{11} mode (the two modes (LP_{11+} , $LP_{11_\times}$) are similarly structured but for a $\pi/2$ rotation).

2. Contrast mechanism

Here, we propose a model for coupling backscattered light with the modes of the FMF. We begin with a general model that we then apply to two specific cases: a single spherical scatterer and a continuous distribution of refractive indices representing biological tissues.

2.1. Coupling model

Illumination is carried out with a particular mode of an MSPL through imaging optics and results in its projection with magnification onto the focal plane and within the sample. Conversely, collecting light with the same optical scheme leads to the projection of backscattered light from the sample onto the fiber tip. As such, backscattered light couples with each of the modes of the

Biomedical Optics EXPRESS

multimode end of the MSPL with different efficiencies. Since the MSPL selectively demultiplexes certain modes, we can directly measure such efficiencies. The rest of the higher-order modes, which are not demultiplexed, couple into the cladding modes of the fiber and are subsequently lost in the first few centimeters of propagation. With a similar approach used in previous studies [8–10], we define the modal coupling efficiency $\boldsymbol{\eta_{l,m}}$ of the incident light field onto LP modes as

$$\boldsymbol{\eta}_{l,m} = \left|\langle \psi \mid \phi_{l,m} \rangle\right|^2 = \underbrace{\left|\iint_s \psi(x,y)^* \phi_{l,m}(x,y) dx dy\right|^2}_{DSR} \tag{1}$$

$$= \underbrace{\left|\iint_\Omega \widetilde{\psi}(\xi,v)^* \widetilde{\phi}_{l,m}(\xi,v) d\xi dv\right|^2}_{FSR} = \left|\langle \widetilde{\psi} \mid \widetilde{\phi}_{l,m} \rangle\right|^2, \tag{2}$$

where $|\phi\rangle$ represents the incident light field state arriving onto the FMF while $|\phi_{l,m}\rangle$ represents the FMF mode state, with l and m being indices associated with LP modes. The second line of the equation is derived from the first using Plancherel's theorem, also called the Parseval-Plancherel identity. Depending on the situation, one can choose to use the direct-space representation (DSR) or the Fourier-space representation (FSR). Here, $\psi(x,y)$ and $\phi(x,y)$ are the direct-space fields, while $\widetilde{\psi}(\xi,v)$ and $\widetilde{\phi}(\xi,v)$ are the spatial Fourier-space fields. The integral index s represents the plane in which the near-field LP modes exist, and its Fourier counterpart Ω represents the solid angle subtended by the NA of the imaging lens. This definition does not account for vector fields and thus, its exactness relies on the scalar approximation, which is usually adequate for most low numerical aperture (NA) imaging systems [11]. From Eq. (2), we observe that each mode added to the system leads to complementary information regarding the SPF as each mode carries an orthogonal projection of the SPF. More specifically, each collected mode allows to sample spatial frequency content of the incident light field. Using this additional information and adequate modeling, we can simultaneously infer certain intrinsic properties of the sample and generate more contrast channels. While the MSPL is wavelength-independent, the modal coupling efficiencies are wavelength-dependent, which may provide an additional way to probe biological samples in a manner similar to light-scattering spectroscopy [12].

To quantitatively estimate spatial frequencies contained in the backscattered wavefront for a given wavelength, we use the SPF that describes the polar distribution of the far-field scattering intensity [13]. For a single spherical scatterer, closed-form solutions arise from Mie scattering theory [14,15], which is particularly useful to validate theoretical predictions. For a distribution of scatterers, empirical phase functions such as the Henyey-Greenstein (HG) distribution [16] are widely used for their approximate representation of tissue scattering and simplified mathematical forms.

2.1.1. Mie scattering coupling

To assess the optical response of the system to a sample and validate the proposed model, we investigated the coupling mechanism for a single scatterer. For spherical dielectrics, Mie scattering theory predicts that the scattering efficiency and phase function depend on the size parameter α defined as

$$\alpha := \pi d/\lambda, \tag{3}$$

where d is the diameter of the spherical scatterer and λ is the wavelength of the impinging field. The SPF is also dependent on the polarization state of the incident light field, but for the sake of conciseness, we only consider linearly polarized illumination. Using a home-made Python

Biomedical Optics EXPRESS

package based on previous studies [17,18] we can compute the parameters $S_{11}(\theta)$ and $S_{22}(\theta)$ which define the far-field phase function for differently-sized dielectric spheres using

$$\begin{pmatrix} E^s_{\parallel} \\ E^s_{\perp} \end{pmatrix} = \frac{e^{-ikr}}{ikr} \begin{pmatrix} S_{11}(\theta) & S_{12}(\theta) \\ S_{21}(\theta) & S_{22}(\theta) \end{pmatrix} \begin{pmatrix} E^0_{\parallel} \\ E^0_{\perp} \end{pmatrix}, \tag{4}$$

where E^s denotes the scattered field while E^0 is the incident field. $E_{\parallel}$ and $E_{\perp}$ are the parallel and perpendicular fields (i.e. two polarization states) measured at a point of distance r from the scatterer, respectively. For spherical scatterers, there is, in theory, no coupling between polarization states and $S_{12} = S_{21} = 0$. We did not take into account the structure of the illuminating field and assumed it to be uniform. Using Eq. (4), we can simulate the full far-field amplitudes profiles (over 4π steradians) for different scatterer sizes as presented in Fig. 2. In Fig. 2(a-c), we present the overlap of the far-field scattering distribution of LP_{01} and LP_{11+} in spatial frequency representation. We notice that the overlap strongly depends on the scatterer size and thus, from Eq. (2), we expect it to affect the modal coupling efficiency. Using the FSR part of Eq. (2), we compute the modal coupling efficiency for a perfectly centered scatterer relative to the collecting mode by computing the overlap integral. In practice, however, it is unlikely that the scattered field will be perfectly axially aligned with the fiber mode field. To account for non-centered scatterers, lateral offsets δ_x and δ_y in the x and y directions, respectively, were added to Eq. (2). Using the convolution theorem, the overlap integral can be computed in Fourier-space as

$$\begin{aligned} \boldsymbol{\eta}_{l,m}\left(\delta_x, \delta_y\right) &= \left|\left\langle \psi\left(x+\delta_x, y+\delta_y\right) \mid \phi_{l,m}(x,y)\right\rangle\right|^2 = |\underbrace{\left[\psi \otimes \phi_{l,m}\right]\left(\delta_x, \delta_y\right)}_{\text{convolution}}|^2 \\ &= \left|\mathscr{F}^{-1}\left\{\widetilde{\psi}(\xi,\nu)\widetilde{\phi}_{l,m}(\xi,\nu)\right\}\left(\delta_x, \delta_y\right)\right|^2. \end{aligned} \tag{5}$$

Equation (5) predicts the modal coupling efficiency of the backscattered light as a function of the lateral offset: Hence, by allowing the imaging system to oversample, we probe each of those offsets to retrieve the scatterer footprint also presented in Fig. 2(a-c). The point spread function (PSF) of such a system is, by definition, the footprint of a sufficiently small scatterer. We therefore define the respective PSF for LP_{01} and LP_{11+} mode as the footprint produced by the 500 nm scatterers shown in Fig. 2(a). We also define the mean modal coupling efficiency as the integral over the lateral offset space

$$\widetilde{\boldsymbol{\eta}}_{\boldsymbol{l,m}} = \left\langle \boldsymbol{\eta}_{l,m}(\delta_x, \delta_y) \right\rangle = \left\langle \left| \widetilde{\psi}(\xi,\nu) \,.\, \widetilde{\phi}_{l,m}(\xi,\nu) \right|^2 \right\rangle_{\Omega}, \tag{6}$$

where $\langle \,.\, \rangle$ represents the average value on the solid angle Ω subtended by the NA of the imaging system. In the modal footprints presented in Fig. 2, some of them appear brighter (or darker) denoting a larger (or lower) mean coupling. The variations of the footprint and mean modal coupling efficiencies as a function of the scatterer diameter shows that the spatially oversampled image carries information in a two-fold manner. In particular, the couple $(\boldsymbol{\eta}_{\boldsymbol{l,m}}(\delta_x, \delta_y), \widetilde{\boldsymbol{\eta}}_{\boldsymbol{l,m}})$ forms the modal signature of the scatterer. With adequate modeling, the analysis of such signature would theoretically allow inferring the geometry of the scatterer, which is a piece of information well below the resolution limit of a typical OCT system.

The oversampled signature also depicts two interesting features. Firstly, the anti-symmetric LP_{11+} mode does not couple near a null offset (i.e. when the scatterer is axially aligned with the fiber mode). This behavior is expected as the phase function for a perfectly spherical scatterer is necessarily symmetric under inversion. Thus, if the scatterer is centered with the collecting mode (null offset), the overlap integral with LP_{11+} (Eq. (2)) should always be zero. Secondly, from

Biomedical Optics EXPRESS

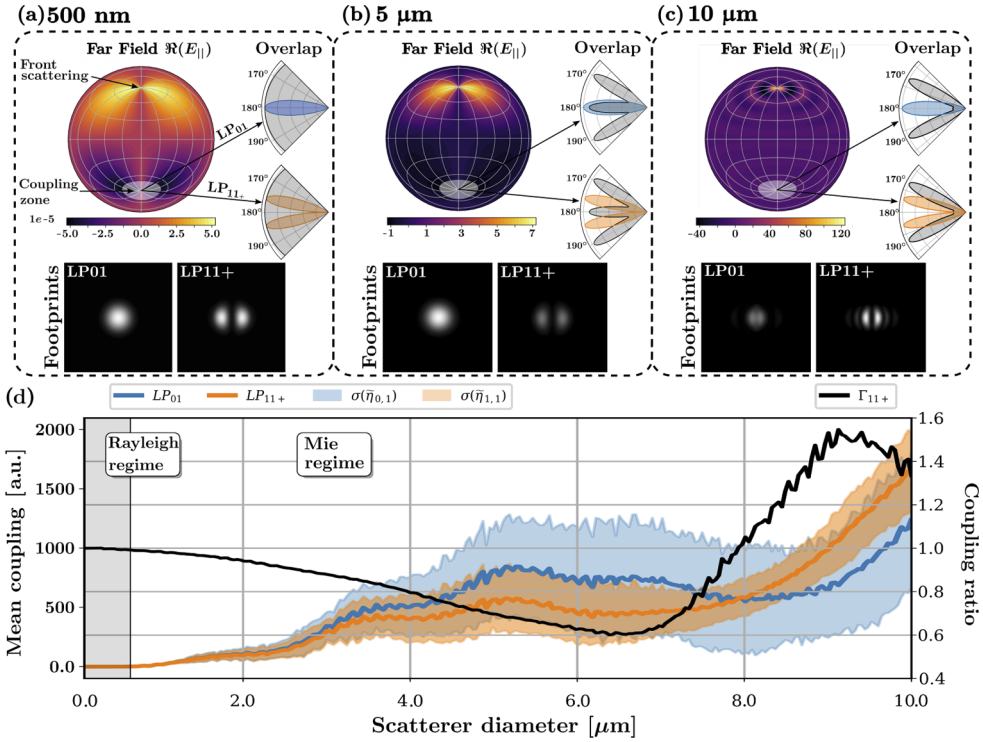

Fig. 2. (a, b & c) Lambert projection of simulated parallel far-field, overlap with LP modes (LP_{01} : blue, LP_{11+} : orange) and simulated modal footprints for scatterers of diameter 500 nm, 5 µm and 10 µm. (d) Mean modal coupling for LP_{01} (blue) and LP_{11+} (orange), and their ratio (black), averaged for the wavelength range of OCT (λ_0 = 930 nm, $\Delta\lambda$ = 50 nm); The x-axis is divided into two sections representing the two scattering regimes, Rayleigh ($\alpha \leq 1$) and Mie ($\alpha > 1$).

Fig. 2(d) we notice that the mean modal coupling efficiencies strongly depend on the scatterer size. However, based on Mie theory, the SPF stabilizes when approaching the Rayleigh regime defined by the size parameter α being inferior to unity. This indicates that modal coupling efficiencies remain relatively constant for small scatterers in comparison to the wavelength. This characteristic can be visualized in Fig. 2(d) presenting the mean modal coupling efficiencies as a function of the scatterer diameter. The solid lines represent the mean coupling averaged over the full OCT spectrum while the color shading represents the standard deviation for that same spectrum. Figure 2(d) also includes the ratio of the modal coupling $\Gamma_{1,1+}$ defined as

$$\Gamma_{11+} = \frac{\widetilde{\eta}_{1,1+}}{\widetilde{\eta}_{0,1}}. \tag{7}$$

We notice that for particles under 2 µm (*i.e.* $\alpha \leq 6.75$ at λ = 930 nm) the ratio LP_{11+} over LP_{01} settles to approximately 1.0 ($\Gamma_{11+} \approx 1.0$). We also remark that the modal coupling is wavelength dependent. This feature is represented as the shaded color ($\sigma(\widetilde{\eta}_{l,m})$) in Fig. 2(d). While this dependency is negligible for scatterers with a diameter under 2 µm, it grows significantly (and almost monotonically) for diameter over that value. Thus, we define the threshold size parameter separating the two regimes as α = 6.75. For large-bandwidth imaging techniques such as OCT, this feature can be of great interest if the response of each wavelength can be efficiently isolated as demonstrated in [19]. Our simulation neglected two important effects: multi-particle

Biomedical Optics EXPRESS

scattering within an optical plane and defocusing. Here, while coherence gating ensures optical sectioning, it does not prevent scatterers to be affected by adjacent particles. Previous work [20] has shown how the SPF of a two-body system varies as a function of the inter-particle spacing. The results demonstrate that the variation of the SPF mainly occurs for large scattering angles and the SPF structure does not change significantly for low angles. As most of OCT imaging system have low NA's, we posit that the presence of multiple scatterers does not affect the structure of the scattered fields, although it would enhance the scattering efficiencies. On the other hand, while the effect of optical defocusing can be emulated by modifying the acceptance cone of the far-field representation of the LP mode, it would also compromise the approximation of the incident plane wave. As such, a more extensive model using the generalized Lorenz-Mie theory would be required to take defocusing into account.

2.2. Coupling mechanism in a biological tissue

In the same way as for Mie scattering, the coupling mechanism for LP modes in biological tissue is directly dependent on the SPF. However, for biological tissues, modeling an accurate phase function for a given sample can prove challenging. The Henyey-Greenstein SPF [16] is widely used as its analytic form simplifies model fitting. It represents an averaged distribution of multi-event scattered photon paths. However, because the photon mean free path in biological samples is an order of magnitude larger than the OCT coherence gating (*i.e.* ≤ 10 μm), most of the photons collected are issued from a single scattering event. For instance, the photon mean free path in human skin is about 350 μm for illumination at 755 nm [21]. The use of a more sophisticated model is thus needed.

A more extensive way to describe a random and continuous medium is to use the refractive index (RI) correlation function $C_n(\rho)$. This function statistically characterizes the structural distribution of RI in the sample. To model $C_n(\rho)$, the Whittle-Matefn (WM) functional family can be used:

$$C_n(\rho) = N_c\, 2^{(5-D)/2}\left(\frac{\rho}{l_c}\right)^{(D-3)/2} K_{(D-3)/2}\left(\frac{\rho}{l_c}\right), \tag{8}$$

where ρ is the radial distance, N_c a scaling factor, D a deterministic factor, l_c the correlation length, and K the Bessel function of the second kind. With this definition for the correlation function and using the first Born approximation [22], one can derive the analytical solution for single-event scattering cross-section per unit of volume $\sigma(\theta, \phi)$ [23,24] such that

$$\sigma(\theta,\phi) = 2\,N_c\,k^4\,l_c^3\,\Gamma(D/2)\frac{(1-\sin^2(\theta)\cos^2(\phi))}{\sqrt{\pi}(1+[2kl_c\sin(\theta/2)]^2)^{D/2}}, \tag{9}$$

where Γ is the gamma function, k is the wavenumber and $(1-\sin^2(\theta)\cos^2(\phi))$ is the dipole factor for a linearly polarized incident field at the angle $\phi = 0$. It is to be noted that the Born approximation is valid under the condition $N_c\,k\,l_c \ll 1$ [22]. The latter condition defines what we refer to as low-coherence samples. Using this model and data provided in [23], we can compute the mean modal coupling in the same way as it was defined in the previous section. Doing so, we observed that for all three parameters (N_c, l_c, D), the mean modal coupling varies in a similar fashion for both modes. For instance, refractive index correlation length (l_c) of a rat liver sample is expected to vary from 2.53 to 5.57 μm [23]. Figure 3 presents the theoretical mean coupling for LP_{01} and LP_{11+} as a function of l_c for such a sample. Figure 3 highlights that the mean coupling $\widetilde{\boldsymbol{\eta}}_{\boldsymbol{l,m}}$ increases almost linearly with l_c for both modes and hence the ratio ($\boldsymbol{\Gamma_{11+}}$) does not change significantly. This behavior is expected as such samples scramble the impinging light field structure, resulting in a loss of spatial coherence. Thus, for samples described per $C_n(\rho)$ the SPF tend to be much smoother than for a single spherical scatterer. As such, we refer to them as low-coherence samples. This result is in contrast with the single scatterer model which predicts large variation of $\boldsymbol{\Gamma_{11+}}$ as a function of the scatterers diameter. Moreover, a low-coherence

Biomedical Optics EXPRESS

sample should not present a characteristic footprint (as opposed to single scatterers) as each point contributes equally to the output image.

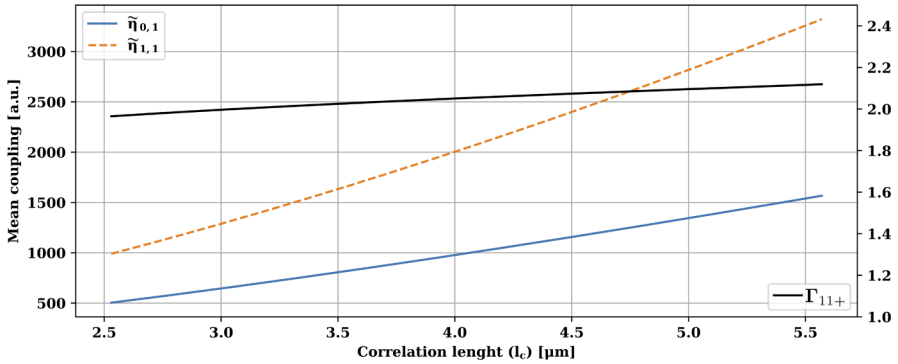

Fig. 3. Theoretical prediction of modal mean coupling in liver sample $\widetilde{\eta}_{l,m}$ (blue & orange) and their ratio Γ_{11+} (black).

Another effect of few-mode coherent imaging is the characteristic speckle pattern associated with each mode. The effect of the illumination pattern on the speckle statistics has been established in [25,26]. More precisely, the speckle autocorrelation function $R_I(\Delta x, \Delta y)$ is linked to the illumination structure as

$$R_I(\Delta x, \Delta y) = \langle I \rangle^2 \left[1 + \left| \frac{\iint |P(\xi,\eta)|^2 \exp\left[i \frac{k}{z} (\xi \Delta x + \eta \Delta y) \right] d\xi d\eta}{\iint |P(\xi,\eta)|^2 d\xi d\eta} \right|^2 \right] \tag{10}$$

where I is the intensity of the incident field, ξ and η are the transverse coordinates at the objective lens plane, Δx and Δy are the transverse coordinates at the image plane, $|P(\xi,\eta)|^2$ is the intensity distribution of the field impinging on the sample, k is the wavenumber, and z is the distance between the lens plane and the image plane. Equation (10) highlights the dependence of speckle pattern on the illumination structure $P(\xi,\eta)$. This model is valid for structured illumination and uniform collection. By using the reciprocity principle of optical scattering processes in turbid media, the model is also valid for uniform illumination and structured collection as discussed previously [27,28]. To some extent, we can consider the LP_{01} illumination as uniform and, hence, we can compute the correlation function for LP_{01} and LP_{11+} imaging. Additionally, it is possible to retrieve a good estimation of the PSF from the speckle pattern on the sample [29].

Previous works have demonstrated the use of an FMF to eliminate spatial coherence of a laser beam in order to even out the speckle pattern [30] or to distribute light intensity around the focal point [31]. However, such multiplexing techniques offer limited control on the modal content in the FMF and are restricted to illuminating or collecting light with a circularly symmetric pattern. This last limitation prohibits evaluating direction sensitive properties. As the MSPL allows precise control over each mode, the asymmetric nature of the LP_{11+} speckle pattern could be used to infer dynamic properties of tissues, such as the direction of flows.

To summarize the theoretical predictions, we have on one hand the single scatterer model which predicts modal coupling efficiency that strongly depends on the scatterer size. On the other hand, we have the low-coherence sample model, which predicts no significant variation on the modal coupling efficiency but a strong variation in the speckle pattern. These theoretical predictions translate to OCT imaging in the following way. We anticipate that low-coherence samples result in OCT images of similar intensity regardless of the imaging mode. However, for samples containing larger scatterers, we expect a size-dependent differential contrast between OCT images produced with each orthogonal mode. This contrast can be used to highlight

Biomedical Optics EXPRESS

large scatterers inside a low-coherence sample as previously reported with neuritic plaque [4]. However, to get a better understanding on the contrast at the frontier, it would be possible to use solution such as finite-difference time-domain (FDTD) [32,33], pseudo-spectral time-domain (PSTD) [34] or even polarization tracking Monte-Carlo simulation [35,36].

3. Materials and methods

3.1. Photonic lantern design

Photonic lanterns achieve mode-mapping through an adiabatic transition between the two ends of the component. A truly adiabatic transition also makes the process lossless. The design of the custom-made MSPL is based on previous work [37] from our group. An extensive description of the fabrication process was also previously reported [38]. The current embodiment uses two different custom-pulled double-clad fibers to produce a strongly asymmetric index profile to build an ultra-short (4 mm long) modally-specific 2-by-1 photonic lantern (see Fig. 1(a)). The short length of the component is a desired feature for imaging as it makes it more robust and resistant to vibrations. The radius of the multimode output of the MSPL is 5.0 μm with a theoretical LP_{01} mode field radius of 4.0 μm and an LP_{11+} mode radius of 4.4 μm.

3.2. Optical system

The MSPL is incorporated into an imaging setup (Fig. 4) consisting of two commercially available spectral-domain (SD) OCT systems (Callisto, Thorlabs, Newton, USA) centered at 930 nm. From the second OCT system, only the spectrometer and acquisition electronics were used for detection – only one OCT source is required for this setup as highlighted in Fig. 4. Its bandwidth of approximately 80 nm provides an axial resolution of 7 μm in the air. This particular system was selected as its wavelength range is within our MSPL operating range. The MSPL features very-low loss over the entire OCT spectrum (under 0.5dB). The FM-OCT system was designed with off-the-shelf optical components including optical fibers (780HP, Thorlabs), achromatic fiber couplers, polarization controllers, B-coated collimators, and achromatic lenses. The objective lens has a 60 mm focal length. In this configuration, illumination is carried out exclusively with LP_{01} . The imaging head is expected to produce a spot-size of approximately 30 μm at the focal point. The optical setup also includes two individual reference arms designed to compensate dispersion and to precisely adjust the zero-delay position for each propagation mode. These adjustments are controlled with optical lengths R_1, R'_1, R_2 and R'_2. The reference arms are adjusted to set an optical path-length difference between the two modes that is a few times longer than the measurement depth of each channel. As such, no crosstalk occurs between the interferometric signals of the individual modes. The $\boldsymbol{\eta_{0,1\rightarrow 0,1}}$ sensitivity was measured to be 92 dB using a mirror and a neutral density filter in the sample arm, as described in [39]. The $\boldsymbol{\eta_{0,1\rightarrow 1,1}}$ sensitivity could not be measured using this standard protocol as no perfect coupling can be achieved between orthogonal modes using a mirror. However, since Fig. 2 demonstrates near perfect mode demultiplexing, and since both modes are processed the same way in the optical setup, we can expect both modal sensitivity to be of the same order of magnitude.

3.3. Data acquisition and post-processing

Raw data acquisition was performed using the proprietary software ThorImageOCT (Thorlabs, USA), which synchronized both spectrometers with the scanning galvanometer system. A custom-made algorithm inspired by previous work [40] was used to correct for background removal, *k*-linearization, dispersion, and to shift the spectrum to precisely adjust the zero-delay position of the two branches at the same axial position. Background removal, *k*-linearization, and dispersion compensation vectors were first computed using the calibration protocol and then applied to LP_{01} and LP_{11+} C-scans individually. Subsequently, a spectrum shift that emulates

Biomedical Optics EXPRESS

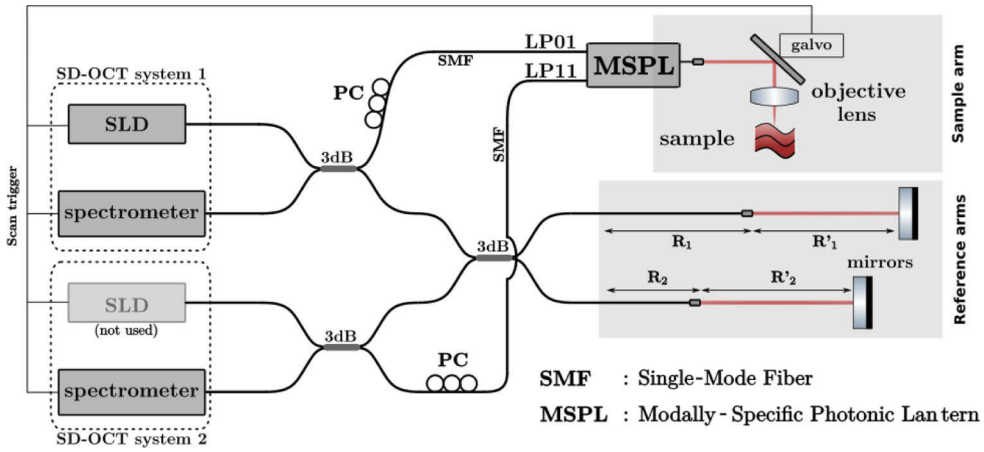

Fig. 4. FM-OCT experimental setup. R_1' and R_2' are the free-space propagation distance while R_1 and R_2 are the fiber propagation distances in each branch. SLD stand for superluminescent diode PC stands for polarization controller, galvo stands for galvanometer-mounted mirrors, and 3dB is for 50:50 fiber couplers.

a zero-delay displacement was applied. The spectrum shift ensures co-localization of both measurements such that pixel-by-pixel comparison of coupling efficiencies is possible. The optimal shift is calibrated prior to the experiment by comparing the two interferograms obtained for both LP modes with a mirror in lieu of the sample. A discrete Fourier transform is applied to retrieve OCT images for each mode and dB scaling is performed. The full calibration and post-treatment algorithm (implemented in Python 3) is available online on a Github repository [41].

3.4. Sample preparation

In order to experimentally study the FM-OCT contrast mechanism, we use three different samples: two microbeads mix and an *ex vivo* sample of rat lung. The first microbead sample is an optical phantom composed of near-infrared transparent polydimethylsiloxane (PDMS) matrix and TiO_2 microbeads (Titanium dioxide powder, Atlantic Equipment Engineers) diameter varying from 0.3 to 10 μm. The sample was prepared with 25 μL of alcoholic solution (70% ethanol) mixed with 15 mg TiO_2 microbeads, 10.6 g of PDMS and 1.5 mL of curing agent in an ultrasonic bath. The second microbead sample was made similarly but adding standard size beads (borosilicate glass, Thermofisher 9008 series, 8.4 μm diameter) to the mix with a mass ratio of 6 part to 1. Finally, the *ex vivo* lung sample was extracted from an adult rat. The lung was not processed prior to imaging.

4. Results

In this section, we report on experimental validation of the demultiplexing scheme and proof-of-concept of the few-mode OCT imaging with a MSPL. In particular, we applied the technique to image two different optical phantoms composed of microbeads and *ex vivo* lung samples.

4.1. Modally-specific photonic lantern validation

To validate the optical behavior of the MSPL with a large bandwidth source, we conducted the experiment with the system described in Fig. 4 but using a mirror in place of the sample. Using the unitary property of the Fourier transform, we can infer the total intensity of the light collected from the interferometric signal returned by the OCT system. Total intensity was measured for

Biomedical Optics EXPRESS

different mirror tilt angles within the range of ±3 degrees. The optical configuration is depicted in Fig. 5(a) where the left part represents the illumination performed using LP_{01} mode (in red). The tilt of the mirror results in a phase shift of the projected LP_{01} mode along the tilt axis causing the mode to transform. The right part of Fig. 5(a) shows the transformed mode coupling with each of the branch of the MSPL (LP_{01} in blue and LP_{11+} in orange). Using the direct-space representation of Eq. (2) the coupling efficiencies can be written down as:

$$\begin{cases} \eta_{0,1\to 0,1}(\theta) = \left|\left\langle \phi_{0,1}(x,y)|\hat{P}(\theta)|\phi_{0,1}(x,y)\right\rangle\right|^2 \\ \eta_{0,1\to 1,1}(\theta) = \left|\left\langle \phi_{0,1}(x,y)|\hat{P}(\theta)|\phi_{1,1}(x,y)\right\rangle\right|^2 \end{cases}, \tag{11}$$

where $\langle\phi_{0,1}|$ is the LP_{01} mode field, $\langle\phi_{1,1}|$ the LP_{11+} mode field, and $\hat{P}(\theta)$ the phase shift operator on the tilt axis $\hat{x}$ with a tilt angle of θ defined as $\hat{P}(\theta) = \exp\{ikx\tan\theta\}$. Those efficiencies were computed for each mode as a function of the tilt angle of the mirror and measured experimentally. Thus, we can validate the mode-field distribution and demultiplexing scheme by comparing the theoretical predictions to the experiment. In particular, for a null mirror tilt angle, we expect no cross-coupling between the modes. This feature is of utmost importance as it certifies that the photonic lantern is indeed modally specific. Figure 5(b) shows theoretical (solid blue and orange lines) and experimental (dotted blue and orange lines) normalized coupling efficiencies of the two modes. Figure 5(c) depicts both modes intensity profiles (LP_{01} and LP_{11+}) as simulated (left) for a perfectly symmetrical FMF and as acquired experimentally (right) at the output of the MSPL. Due to the asymmetric nature of our home-made MSPL, the resulting mode fields are not exactly the same as would be expected of a circularly symmetric FMF fiber. These differences can be visualized by comparing the left and right columns of Fig. 5(c) where the experimental LP_{01} and LP_{11+} modes are slightly elongated with respect to the simulated modes for a perfectly symmetric FMF.

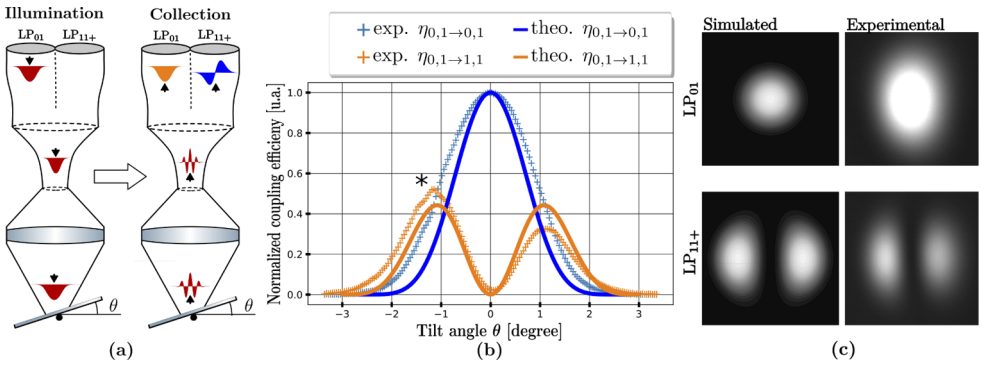

Fig. 5. Validation of the demultiplexing scheme. (a) Optical setup consisting of the MSPL, an imaging lens and tilted mirror for illumination (left) and detection (right). (b) Theoretical (solid lines) and experimental (dashed lines) coupling efficiencies for LP_{01} (blue) and LP_{11+} (orange). (c) Simulated and experimental intensity profiles of the output face of the MSPL, for each mode. The asterisk highlights a notch in the left lobe of the experimental coupling $\eta_{0,1\to 1,1}$.

4.2. Phantom imaging

The optical response of a phantom made of microbeads was acquired and analyzed using LP_{01} for illumination and both LP_{01} and LP_{11+} for collection. Figure 6(a to d) show collected scans using LP_{01} (top) and LP_{11+} (bottom) modes displayed in logarithmic scale. While Fig. 6(a,

Biomedical Optics EXPRESS

b & c) presents results obtained using disperse beads (diameter ranging from 0.3 to 10 μm), sub-figure (d) was acquired using a mixture of standard size beads (8.3 μm) and the disperse beads. Figure 6(a) shows *en face* maximum intensity projection (MIP) of the C-scans collected with LP_{01} and LP_{11+}. Figure 6(b) presents a B-scan taken from the same region of interest (ROI) of the optical phantom with enlarged insets (i and ii). The visible structures (white arrows) appearing in Fig. 6(a & b) point at a non-uniform mixture of the microbeads in the phantom. Figures 6(c & d) show two oversampled (by a factor of ≈ 15) MIPs from two optical phantoms obtained at similar resolution. The first one (c) is made of disperse beads and the second one (d) is made of a mixture of standard size and disperse beads with the proportion being six parts to one, respectively. It should be pointed out that the contrast of the two images is adjusted for saturation not to occur. Hence, the few scatterers that strongly couple with LP_{11+} in Fig. 6(d) tend to dim the others. The mixed sample is thus majorly constituted of exactly 8.3 μm beads with a small proportion of beads over and below that size. This sample was produced in order to highlight a size-selective contrast mechanism. Sub-figures (c & d) also include red and blue arrows pointing at specific microbeads for comparison between the two modes. In addition to highlighting the selective contrast, oversampled images show the experimental footprints of scatterers for each mode: a single lobe for LP_{01} and a double-lobe for LP_{11+}. In particular, the red arrows show scatterers with a higher coupling efficiency in the LP_{01} mode compared to LP_{11+} mode, while the blue arrows indicate the opposite pattern (lower efficiency).

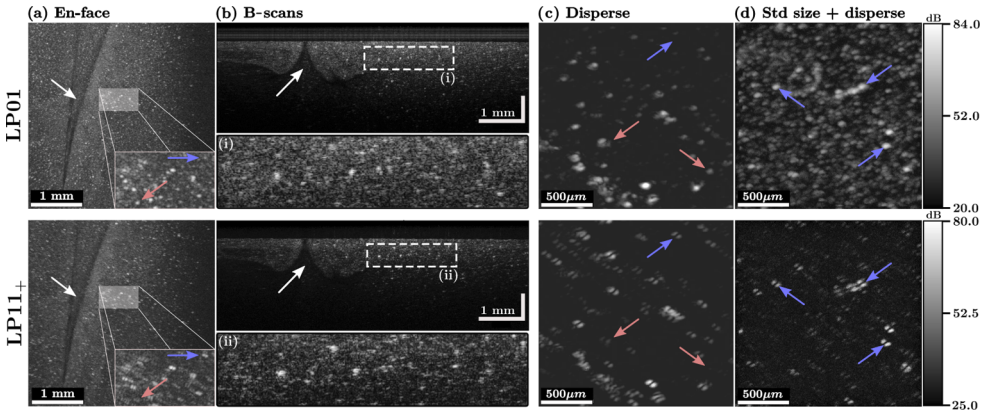

Fig. 6. FM-OCT scans of a microbead optical phantom using LP_{01} (top) and LP_{11+} (bottom). (a) Maximum intensity projection (MIP) of *en-face* view. (b) B-scans obtained using LP_{01} and LP_{11+} with enlarged insets (i & ii). (c-d) Oversampled and zoomed C-scan obtained using disperse TiO_2 microbeads (0.3-10 μm) and mono-disperse borosilicate glass beads (8.3 μm), respectively. Sub-figures (d) are presented with their respective logarithmic scale bars.

4.3. *Rat lung imaging*

The optical response of an *ex vivo* rat lung was acquired and analyzed using LP_{01} illumination and both LP_{01} and LP_{11+} for collection. The top row shows images collected with LP_{01}, while the bottom row shows images acquired with LP_{11+}. Figures 7(a & b) show B-scans and *en face* view of a freshly excised *ex vivo* rat lung. Two structures, marked with white arrows, can be observed in the images. Fig. 7(a & b) show the lung pleura at the air-tissue interface as well as an alveolus. For each collection mode, ROIs were selected, enlarged, and reproduced as insets (i-v) of the corresponding *en face* views. Insets (i-iv) display some of the regions where differential contrasts were observed. In the insets (i-iv), the blue arrows highlight higher LP_{01} mean coupling efficiencies ($\widetilde{\eta}_{0,1}$) while red arrows point to higher LP_{11+} mean coupling efficiencies ($\widetilde{\eta}_{1,1+}$) The

Biomedical Optics EXPRESS

red arrows also highlight the double-lobe pattern predicted for single spherical scatterers. While the double-lobe pattern does not certify the presence of a single spherical scatterer, it does ensure a symmetrical structure as discussed in Section 2.1.1. Inset (v) shows homogeneous regions of the rat lung highlighting the speckle pattern of the OCT image. The autocorrelation of the speckle pattern of (iv) is presented in column (b) along with respective theoretical predictions (top right corner) obtained using Eq. (10) for a large bandwidth OCT light source.

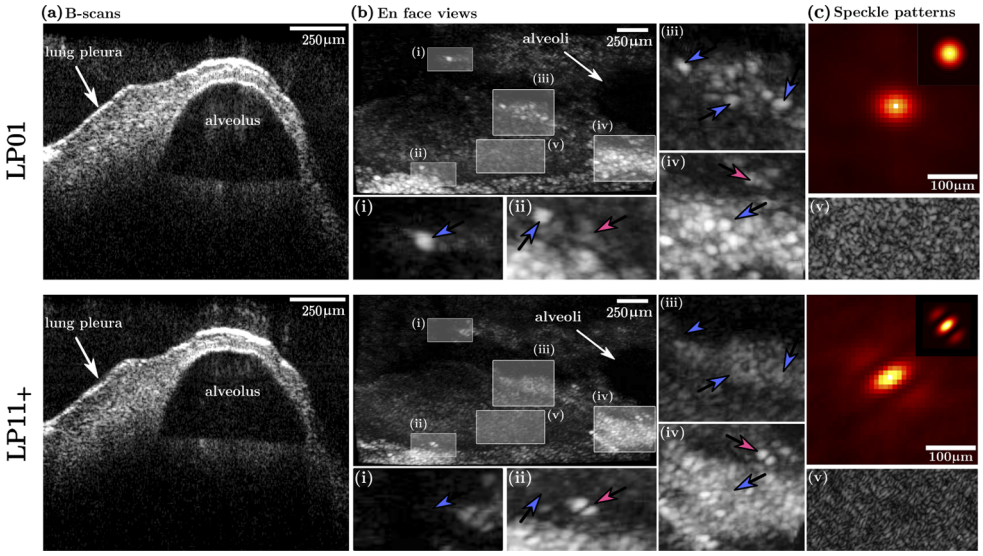

Fig. 7. Adult rat lung imaged with FM-OCT (dB scaling). (a) B-scan of a rat lung using LP_{01} (top row) and LP_{11+} (bottom row). (b) *En-face* view MIP of a rat lung with insets (i-iv) enlarged. Inset (v), reproduced to the right, shows the speckle pattern. (c) Auto-correlation function of speckle pattern with the predicted pattern integrated of the OCT wavelength range (inset).

5. Discussion

By combining the coherence gating of OCT with a phase function demultiplexing scheme, FM-OCT unravels the possibility to study unexplored contrast channels. Our approach is based on the use of modally-specific photonic lantern, which allows to efficiently demultiplex and measure mode-coupled backscattered light without compromising OCT signal quality. The proposed optical system (Fig. 4) enables parallelization of the measurements, a tight control over dispersion, and OCT zero-delay localization for both modes. These characteristics ensure an optimal co-registration of images for all contrast channels. Moreover, the implementation does rely on off-the-shelf optical components with the only exception being the modally-specific photonic lantern itself, which was custom-made for this application.

In our first experiment, a tilted mirror was used to investigate mode coupling. The analysis of the results validates the propagation modes demultiplexing process in three points: it (1) shows the correspondence between the MSPL modes and the theoretical FMF mode, (2) demonstrates a mode demultiplexing as theoretically predicted, and (3) highlights a very low crosstalk for a zero tilt angle, which was demonstrated by $\boldsymbol{\eta_{0,1\rightarrow 1,1}(0)} \approx 0$ (see Fig. 5(b)). However, the small degree of asymmetry of the $\boldsymbol{\eta_{0,1\rightarrow 1,1}}$ and the wider coupling $\boldsymbol{\eta_{0,1\rightarrow 0,1}}$ indicates a slight deviation from the ideal LP modes of an FMF. Additionally, we notice a notch on top of the left lobe of $\boldsymbol{\eta_{0,1\rightarrow 1,1}}$ (highlighted with an asterisk). This notch is caused by the residual influence of one of the fiber cores which are supposed to vanish in the tapering process. Such minor aberrations can

Biomedical Optics EXPRESS

be corrected through design and fabrication improvements of the MSPL, which we will integrate into future developments.

In this work, we also developed and validated a simple model to compute modal coupling efficiencies through the study of *in vitro* and *ex vivo* samples. The study of the optical response of microbeads of varying diameters (ranging from 0.3 to 10 μm) validates two predictions of the coupling model. First, Fig. 6(a & b) shows specific scatterers that appeared brighter when imaged with LP_{11+} compared to LP_{01} (red arrows) and vice-versa (blue arrows). Additionally, from Mie scattering theory, we know that larger scatterers also have higher scattering efficiencies and hence produce brighter spots in OCT scans. As we demonstrated, scatterers with small diameters ($\leq$ 2μm) tend to couple equivalently in both modes while those with a diameter superior to that value tend to couple more into the LP_{11+} mode. Therefore, the coupling model predicts that brighter spots in LP_{01} imaging tend to appear even brighter in LP_{11+} (red arrows for enhanced coupling). Also, to avoid signal saturation, the non-enhanced scatterer simply appeared dimmer. On the other hand, scatterers marked with blue arrows indicate diminished LP_{11+} coupling and can be associated with scatterers with a diameter comprised in the range of 3 - 7 μm for which the coupling ratio (Γ_{11+}) is below 1 (Fig. 2(d)). Results obtained with standard size beads (Fig. 6(d)) also highlights a consistent coupling mechanism as most of the beads (majorly composed of standard size 8.3μm) couple with the same ratio in both LP_{01} and LP_{11+} modes. Additionally, LP_{11+} images obtained from the microbead phantom (Fig. 6(a & c)) feature the predicted double-lobe footprint (Fig. 2). The results obtained from the microbead phantom validates the predicted modal signature and demonstrates the possibility of discriminating scatterers based on their size. While we did not yet investigate the optical response of a large set of mono-dispersed scatterers, this modal signature could be of great interest for sub-resolution sensing, in particular when high sensitivity to scatterer size is relevant. Techniques such as elastic light scattering spectroscopy [2] or inverse spectroscopic optical coherence tomography [23] indeed exploit nuclear-to-cytoplasmic volume ratios to discriminate cancerous versus normal tissues.

The investigation of the lung sample shows that most of the latter fall within the regime of a low-coherence sample for which differential coupling was not observed ($\Gamma_{11+} \approx$ *constant*). This observation is consistent with the model description in which the phase function derived from the Born approximation (Eq. (9)) is uniform enough for the coupling to be equal for both modes (LP_{01} and LP_{11+}). There are however several areas (as shown in Fig. 7(b) insets) for which differential coupling is observed. This is expected as for the porous trait of the lung structures [42,43]. The differential coupling can thus be associated to high refractive index heterogeneities such as capillaries or cell clusters having a size parameter larger than the threshold value (α>6.75). Some of those particular areas presented in Fig. 6(a) insets also feature the double-lobe pattern specific to single spherical scatterers. The double-lobe pattern also indicates a symmetric structure and therefore supports the hypothesis of cell clusters. No comparison was yet done with histology, which will be integrated into future research. Results from the microbeads phantom and low-coherence sample underline an interesting feature. Small scatterers and low-coherence samples correspond to low RI correlation lengths and do not feature differential coupling between the two modes. However, in some areas, high RI correlation lengths, originating from structures such as large scatterers produce a differential coupling between the two modes and generate an important source of contrast for OCT. This contrast is based on the size parameter (a combination of scatterer diameter and wavelength) which allows for a certain tunability for highlighting biological structures of interest. These results validate the proposed model and corroborate previously reported results [4]. Moreover, as theoretically predicted, the speckle pattern was very distinctive of the fiber mode with which each image was acquired. We notice that the image obtained with LP_{11+} is less affected by the speckle as its structure is finer than the speckle pattern of LP_{01} . Finally, the speckle autocorrelation associated with each mode was experimentally

Biomedical Optics EXPRESS

measured and compared to theoretical predictions (Fig. 7(b)). While results for each mode are concordant, the experimental measurement for LP_{11+} shows dimmer side lobes compared to what would be expected.

In summary, we demonstrated a new and efficient technique of studying the optical response of samples using different types of structured light field (LP modes). Additionally, we proposed and validated a simple coupling model that described a contrast based on the refractive index correlation length, which is a mechanism that had already been exploited [4] but not fully characterized. Our work shows that FM-OCT's advantage over conventional OCT is in locating larger cells or clusters of proteins, such as found in amyloid plaques in the brain, in a background of rather homogeneous tissue. Indeed, Fig. 2(c) suggests that the contrast between the two modes is null in the Rayleigh regime, and becomes significant in the Mie regime, especially as the particle size reaches several wavelengths. Furthermore, we provided a proof-of-principle based on a novel modally-specific photonic lantern that allowed for an all-fiber optical circuit. The all-fiber approach permits adding channels without compromising signal quality: indeed, one could now envision scaling up the number of channels with the development of 3- to N-fiber MSPLs. Despite its highly efficient demultiplexing scheme, the proposed optical setup presented some technical limitations. OCT imaging was performed at a wavelength accommodating the operating wavelength of the MSPL, for which devices such as broadband circulators are not common. Following this proof-of-principle, custom fibers will be drawn to design an MSPL at longer wavelength for OCT imaging (e.g. 1300 nm). In addition to allow for better penetration, an MSPL operating at longer wavelengths could be coupled with circulators and integrated in a swept-source OCT system, using two photodetectors (in lieu of spectrometers), for parallel acquisition of the modes; or even a single photodetector coupled to an optical switch for sequential acquisition of the modes. Also, in the situation where the collecting mode does not feature a rotational symmetry, the polarization state of the incident light field can affect the coupling (*e.g.* microbeads imaging). Future work includes *in vivo* validation of the contrast mechanism in biological tissue.

Funding. Fonds de Recherche du Québec - Santé (32600); Natural Sciences and Engineering Research Council of Canada (RGPIN-06404-2016, RGPIN-2015-04672, RGPIN-2018- 06151, RTI-2016-00636).

Acknowledgements. We thank Xavier Attendu for his precious help with the redaction of the manuscript, and Emilie Heckel and Irène Londono for sample preparation.

Disclosures. CB, NG: Castor Optics, inc. (I,P), MPdSH, SBB (P)

Data availability. Data underlying the results presented in this paper are not publicly available at this time but may be obtained from the authors upon reasonable request.

References

1. D. Huang, E. A. Swanson, C. P. Lin, J. S. Schuman, W. G. Stinson, W. Chang, M. R. Hee, T. Flott, K. Gregory, C. A. Puliafito, and J. G. Fujimoto, "Optical coherence tomography," Science **254**(5035), 1178–1181 (1991).
2. I. Georgakoudi, B. C. Jacobson, J. V. Dam, V. Backman, M. B. Wallace, M. G. Müller, Q. Zhang, K. Badizadegan, D. Sun, G. A. Thomas, L. T. Perelman, and M. S. Feld, "Fluorescence, reflectance, and light-scattering spectroscopy for evaluating dysplasia in patients with barrett's esophagus," Gastroenterology **120**(7), 1620–1629 (2001).
3. I. Itzkan, L. Qiu, H. Fang, M. M. Zaman, E. Vitkin, I. C. Ghiran, S. Salahuddin, M. Modell, C. Andersson, L. M. Kimerer, P. B. Cipolloni, K.-H. Lim, S. D. Freedman, I. Bigio, B. P. Sachs, E. B. Hanlon, and L. T. Perelman, "Confocal light absorption and scattering spectroscopic microscopy monitors organelles in live cells with no exogenous labels," Proc. Natl. Acad. Sci. **104**(44), 17255–17260 (2007).
4. P. Eugui, A. Lichtenegger, M. Augustin, D. J. Harper, D. J. Muck, T. Roetzer, A. Wartak, T. Konegger, G. Widhalm, C. K. Hitzenberger, A. Woehrer, and B. Baumann, "Beyond backscattering: optical neuroimaging by BRAD," Biomed. Opt. Express **9**(6), 2476–2494 (2018).
5. P. Eugui, C. Merkle, D. J. Harper, A. Lichtenegger, M. Augustin, M. Muck, A. Wöhrer, C. K. Hitzenberger, and B. Baumann, "Simultaneous bright and dark field OCT with a polarization sensitive detection," in *Optical Coherence Tomography and Coherence Domain Optical Methods in Biomedicine XXIII*, vol. 10867 J. G. Fujimoto and J. A. Izatt, eds., International Society for Optics and Photonics (SPIE, 2019).
6. A. W. Snyder and J. Love, *Optical Waveguide Theory* (Springer, 1983), 1st ed.

Biomedical Optics EXPRESS

7. T. A. Birks, I. Gris-Sánchez, S. Yerolatsitis, S. G. Leon-Saval, and R. R. Thomson, "The photonic lantern," Adv. Opt. Photonics **7**(2), 107–167 (2015).
8. Y. Cotte, M. F. Toy, N. Pavillon, and C. Depeursinge, "Microscopy image resolution improvement by deconvolution of complex fields," Opt. Express **18**(19), 19462–19478 (2010).
9. K. Kataoka, "Estimation of coupling efficiency of optical fiber by far-field method," Opt. Rev. **17**(5), 476–480 (2010).
10. A. Fardoost, H. Wen, H. Liu, F. G. Vanani, and G. Li, "Optimizing free space to few-modefiber coupling efficiency," Appl. Opt. **58**(13), D34–D38 (2019).
11. B. W. Smith, D. G. Flagello, J. R. Summa, and L. F. Fuller, "Comparison of scalar and vector diffraction modeling for deep-UV lithography," in *Optical/Laser Microlithography*, vol. 1927 J. D. Cuthbert, ed., International Society for Optics and Photonics (SPIE, 1993), pp. 847–857.
12. V. Backman, R. Gurjar, K. Badizadegan, I. Itzkan, R. R. Dasari, L. T. Perelman, and M. S. Feld, "Polarized light scattering spectroscopy for quantitative measurement of epithelial cellular structures in situ," IEEE J. Sel. Top. Quantum Electron. **5**(4), 1019–1026 (1999).
13. S. K. Sharma, *A Review of Approximate Analytic Light-scattering Phase Functions* (Springer Berlin Heidelberg, 2015), pp. 53–100.
14. S. L. Jacques, "Optical properties of biological tissues: a review," Phys. Med. Biol. **58**(11), R37–R61 (2013).
15. C. Bohren and D. R. Huffman, *Angular Dependence of Scattering* (John Wiley & Sons, Ltd, 2007), chap. 13, pp. 381–428.
16. L. G. Henyey and J. L. Greenstein, "Diffuse radiation in the Galaxy," Astrophys. J. **93**, 70–83 (1941).
17. C. F. B. D. R. Huffman, *Particles Small Compared with the Wavelength* (John Wiley & Sons, Ltd, 1998), chap. 5, pp. 130–157.
18. B. J. Sumlin, W. R. Heinson, and R. K. Chakrabarty, "Retrieving the aerosol complex refractive index using Pymiescatt: a Mie computational package with visualization capabilities," J. Quant. Spectrosc. Radiat. Transfer **205**, 127–134 (2018).
19. R. Leitgeb, M. Wojtkowski, A. Kowalczyk, C. K. Hitzenberger, M. Sticker, and A. F. Fercher, "Spectral measurement of absorption by spectroscopic frequency-domain optical coherence tomography," Opt. Lett. **25**(11), 820–822 (2000).
20. L.-H. Tsai, P. N. Yang, C.-C. Wu, and H. Y. Lin, "Quantifying scattering coefficient for multiple scattering effect by combining optical coherence tomography with finite-difference time-domain simulation method," J. Biomed. Opt. **23**(8), 086004 (2018).
21. R. Eze and S. Kumar, "Laser transport through thin scattering layers," Appl. Opt. **49**(3), 358–368 (2010).
22. V. Backman, A. Wax, and H. Zhang, *A Laboratory Manual in Biophotonics* (CRC Press, 2017).
23. J. Yi and V. Backman, "Imaging a full set of optical scattering properties of biological tissue by inverse spectroscopic optical coherence tomography," Opt. Lett. **37**(21), 4443–4445 (2012).
24. S. K. Sharma, *Elastic Scattering of Electromagnetic Radiation: Analytic Solutions in Diverse Backgrounds* (CRC Press, 2018).
25. B. Frieden, "Laser speckle and related phenomena," IEEE J. Quantum Electron. **20**(12), 1533 (1984).
26. X. Hu, M.-X. Dong, Z.-H. Zhu, W. Gao, and C. Rosales-Guzmán, "Does the structure of light influence the speckle size?" Sci. Rep. **10**(1), 199 (2020).
27. A. Kokhanovsky, "Volume 4: Light scattering and radiative transfer," in *Springer Series in Light Scattering*, A. A. Kokhanovsky, ed. (Springer, 2019).
28. R. Potton, "Reciprocity in optics," Rep. Prog. Phys. **67**(5), 717–754 (2004).
29. N. Meitav, E. Ribak, and S. Shoham, "Point spread function estimation from projected speckle illumination," Light: Sci. Appl. **5**(3), e16048 (2016).
30. E. Auksorius, D. Borycki, and M. Wojtkowski, "Multimode fiber enables control of spatial coherence in Fourier-domain full-field optical coherence tomography for in vivo corneal imaging," Opt. Lett. **46**(6), 1413–1416 (2021).
31. J. Kim, E. K. Kim, D. T. Miller, and T. E. Milner, "Speckle reduction in OCT with multimode source fiber," in *Optical Fibers and Sensors for Medical Applications IV*, vol. 5317 I. Gannot, ed., International Society for Optics and Photonics (SPIE, 2004), pp. 246–250.
32. O. Romanov, A. Tolstik, N. Ortega-Quijano, F. Fanjul-Velez, and J. Arce-Diego, "Finite-difference time-domain simulation of light propagation in 2D scattering media," Nonlinear Phenom. Complex Syst. **12**, 267–274 (2009).
33. R. A. Drezek, A. Dunn, and R. Richards-Kortum, "Light scattering from cells: finite-difference time-domain simulations and goniometric measurements," Appl. Opt. **38**(16), 3651–3661 (1999).
34. Q. H. Liu, "The pseudospectral time-domain (PSTD) method: a new algorithm for solutions of Maxwell's equations," in *IEEE Antennas and Propagation Society International Symposium 1997. Digest*, vol. 1 (1997), pp. 122–125 vol.1.
35. G. Carles, P. Zammit, and A. R. Harvey, "Holistic monte-carlo optical modelling of biological imaging," Sci. Rep. **9**(1), 15832 (2019).
36. Y. Wang and L. Bai, "Accurate monte carlo simulation of frequency-domain optical coherence tomography," Int. J. for Numer. Methods Biomed. Eng. **35**(4), e3177 (2019).
37. N. Godbout and S. Bolduc Beaudoin, "Multi-clad optical fiber with taper portion, and optical fiber device having same. wo patent 2019148276a1," (2019).
38. S. B. Beaudoin, "Révision du processus de fabrication de coupleurs fusionnés á quelques fibres," Master's thesis, École Polytechnique de Montréal (2018).

Biomedical Optics EXPRESS

39. R. Leitgeb, C. K. Hitzenberger, and A. F. Fercher, "Performance of fourier domain vs. time domain optical coherence tomography," Opt. Express **11**(8), 889–894 (2003).
40. X. Attendu, R. M. Ruis, C. Boudoux, T. G. van Leeuwen, and D. J. Faber, "Simple and robust calibration procedure for k-linearization and dispersion compensation in optical coherence tomography," J. Biomed. Opt. **24**(5), 1–11 (2019).
41. M. Poinsinet de Sivry-Houle, "MartinPdeS/PyMieSim: First release of Mie Scattering simulation software PyMieSim," https://doi.org/10.5281/zenodo.4556074 (2021).
42. B. Lande and W. Mitzner, "Analysis of lung parenchyma as a parametric porous medium," J. Appl. Physiol. **101**(3), 926–933 (2006).
43. M. S. Durkee, G. K. Fletcher, C. Carlson, K. Matheson, S. K. Swift, D. J. Maitland, J. D. Cirillo, and K. C. Maitland, "Light scattering by pulmonary alveoli and airway surface liquid using a concentric sphere model," Opt. Lett. **43**(20), 5001–5004 (2018).